Earth, Planets and Space

FULL PAPER Open Access

Comparisons of in situ ionospheric density using ion velocity meters onboard FORMOSAT-7/COSMIC-2 and ICON missions

Jong-Min Choi[1], Charles Chien-Hung Lin[1*], Rajesh Panthalingal Krishanunni[1], Jaeheung Park[2,3], Young-Sil Kwak[2,3], Shih-Ping Chen[1], Jia-Ting Lin[1] and Min-Ti Chang[4]

Abstract

We report the preliminary inter-satellite comparisons of the in situ ion density measurements by the ion velocity meter (IVM) onboard FORMOSAT-7/COSMIC-2 (F7/C2) and Ionospheric Connection Explorer (ICON) missions, during the solar minimum period of December 2019 to November 2020. The initial comparisons reveal identical diurnal, seasonal, and latitude/longitude variations in the two ion-density measurements, with F7/C2 consistently yielding stronger values than ICON, which could partly result from the difference in their orbit altitudes. The diurnal variation in the equatorial region did not show any effect of pre-reversal enhancement (PRE) during 2019–2020. The daytime plasma distributions show larger ion densities over a narrow latitudinal belt around the geomagnetic equator in all seasons, and the low-latitude densities reveal signatures of hemispherical asymmetry, with larger values occurring in the summer hemisphere. The observations also reveal distinct wavenumber-4 longitudinal modulation, which is most prominent in equinox and becomes less distinguishable during December solstice months. The simultaneous observations from F7/C2 IVM and ICON IVM also provide opportunities to study the spatial configuration and time evolution of ionospheric irregularities in the equatorial and low latitude regions. The F7/C2 and ICON simultaneously observed the equatorial plasma bubbles (EPBs) occurring around Taiwan on 18 October 2020, and the observations are consistent with each other. The EPBs were also observed by an all-sky imager located in Taiwan, comparing the satellite observations.

Key points

1. F7/C2 IVM shows similar patterns of diurnal, seasonal and latitude/longitude variations of ion density to ICON IVM but with stronger magnitudes.
2. Distinct latitudinal and longitudinal variations of plasma distributions along seasons were observed during 2019-2020.
3. Simultaneous observations by the multi-satellite constellation of F7/C2 and ICON and all-sky imager provide opportunity to monitor evolutions of EPBs.

Keywords FORMOSAT-7/COSMIC-2, ICON, IVM ion density, Solar minimum, Equatorial plasma bubble

*Correspondence:
Charles Chien-Hung Lin
charles@mail.ncku.edu.tw
Full list of author information is available at the end of the article

Graphical Abstract

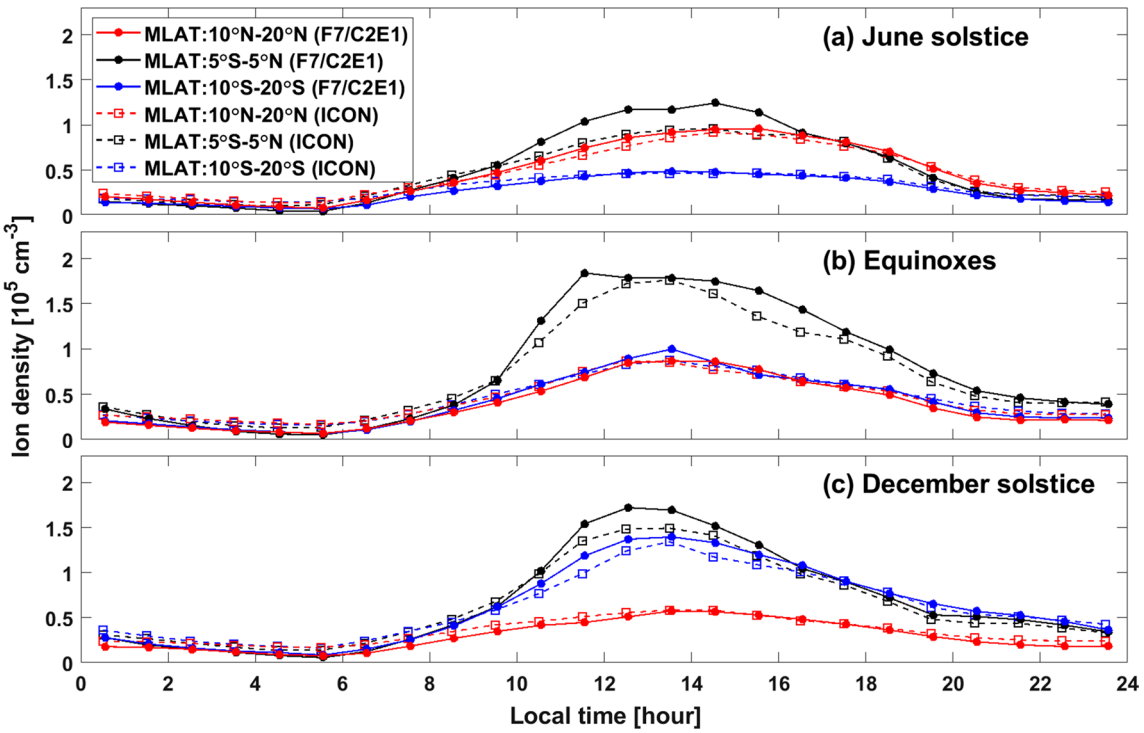

Introduction

The Ion Velocity Meter (IVM) instruments onboard FORMOSAT-7/COSMIC-2 (F7/C2) constellation and Ionospheric Connection Explorer (ICON) satellite are conducting in situ measurements of ion density in the topside F region (Immel et al. 2018; Chu et al. 2021; Chen et al. 2021; Chou et al. 2021a; Derghazarian et al. 2021). With the IVM mounted on each satellite, the six F7/C2 satellites can observe ionospheric irregularities events with a wide coverage. The simultaneous observations of F7/C2 IVM and ICON IVM provide unprecedented opportunities to study ionosphere dynamics and irregularities through coordinated observations from multiple satellites.

It is well known that the extreme ultraviolet (EUV) solar radiation strongly influences the generation the ionospheric plasma density through the production of ion–electron pairs. The plasma density increases as the sun rises and reaches a maximum around 1300–1400 LT. As the solar zenith angle increases after noon, plasma production gradually decreases. Therefore, the ionospheric plasma density is affected by solar EVU and shows a noticeable variation with a diurnal cycle. The temporal variations of the Earth's ionosphere are ultimately linked to those of solar activity, because the main source of the ionospheric plasma is photoionization of neutrals by solar EUV and X-ray radiations.

Solar activity in the years 2007–2009 was unexpectedly low, as evidenced by the extremely low levels of solar EUV radiation and the F10.7 index. The ionospheric response to the extremely low solar activity has been reported and compared to that of the previous solar activity (e.g., Chen et al. 2011; Emmert et al. 2010; Heelis et al. 2009; Liu et al. 2011; Lühr and Xiong 2010; Solomon et al. 2010). Heelis et al. (2009) reported the unusual behavior of O+/H+transition height using the Communications/Navigation Outage Forecasting System (C/NOFS) satellite and suggested that the ionosphere significantly contracted over the period from June to August 2008. Lühr and Xiong (2010) showed that the IRI-2007 model prediction was much higher than the electron density of Challenging Minisatellite Payload or CHAMP (400 km in altitude) and Gravity Recovery and Climate Experiment or GRACE (500 km in altitude) satellite during the solar minimum period. The F10.7 solar activity index for 2019–2020, when F7/C2 and ICON were operating normally, is similar to that of 2007–2009. In this paper, we investigate by comparing inter-satellite observation of the topside F region ion density of F7/C2 IVM and ICON IVM during the recent solar minimum period.

As the in situ ion density measurements by the low-latitude satellites are very useful for the study of the plasma irregularities or mainly the equatorial plasma bubble (EPB), having the constellations of six F7/C2 and an ICON satellites will provide previously unavailable consecutive in situ observations of the EPB over the same region. An EPB generally signifies a localized region of plasma depletion relative to the ambient plasma density. The severe ionospheric turbulence by EPB affects the path of radio waves in the ionosphere, causing problems in communication and navigation systems. After sunset, the gradient of plasma density in the bottomside F region increases steeply with altitude, affecting the growth of the Rayleigh–Taylor instability (RTI). EPB is generated from unstable ionospheres due to the growth of RTI (c.f. Sultan 1996; Kelley 2009). The EPBs occur in the equatorial F region after sunset and are elongated along the magnetic field lines (e.g., Kil et al. 2004; Martinis and Mendillo 2007; Chou et al. 2021b). The C/NOFS satellite operated in a low inclination (13°) and elliptical (400–800 km) orbit during 2008–2015. In situ satellite measurements of C/NOFS IVM conducted the characteristics and generation of EPB during the long solar minimum (e.g., Huang et al. 2013, 2014; Huang 2017; Kil et al. 2011a, 2015). The EPB occurrence rates are maximum for 20–22 LT (e.g., Su et al. 2006). However, strong postmidnight EPBs are also observed during the June solstice of the solar minimum (e.g., Hei et al. 2014; Yizengaw et al. 2009, 2013).

F7/C2 was launched on 25 June 2019 into a low inclination (24°) at ~ 550 km altitude (Lin et al. 2020). The ICON was launched on 11 October 2019. The satellite has a circular low inclination orbit (27°) at an altitude of ~ 600 km (Immel et al. 2018, 2021). F7/C2 IVM and ICON IVM measured the ion density, velocities, temperature, and composition (Heelis et al. 2017). The IVM separately outputs the fractional ion densities of O^+ and H^+ as well as the net ion density of all the plasma constituents (i.e., the total ion density). In this study, we used the total ion density product from December 2019 to November 2020. To cross-validate the data of the two satellites, we compare diurnal, seasonal and latitudinal variations of the ionospheric density. An EPB event simultaneously observed by the consecutive orbit crossings of the seven satellite constellation on 18 October 2020 are examined. Consecutive orbits provide potential of detecting the evolution of the EPBs in the region to identify the characteristics. Concurrent all sky imager observations are used to confirm and compare with the in situ EPB observation. The data selection for this paper is described in "Data selection" section. The observation results are given in "Diurnal variation of ion density" and "Simultaneous observations of equatorial plasma bubbles (EPBs)" sections. Finally, we draw our main conclusions in "Conclusions" section.

Data selection

By comparing the in situ ion densities obtained from the IVM on board equatorial satellite#1 of F7/C2 (simplified as F7/C2E1) and ICON, respectively, we investigate the diurnal, seasonal, and longitudinal variations of ion density from December 2019 to November 2020 and an EPB event observed around Taiwan on 18 October 2020. For comparison with ICON, only a single F7/C2 satellite is used because it descended into final mission orbit first. Figure 1 shows the daily averaged F10.7 and Kp index. The solar flux values were very low (< 100 sfu) in 2018–2020, and its magnitude is similar to the low solar flux in 2008–2010. By August 2020, the solar flux increased to 100, and then it seems to rise slightly. This study uses the F7/C2 ivmLm2 product and version 6 of the ICON Level-2 data, and only magnetically quiet days ($Kp \leq 3$) during the selected period are considered for the analyses. Figure 2 shows the data availability distributions of F7/C2E1 data (red) and ICON data (blue) as a function of local time (1 h bin) for June solstice (May, June, July, and August: top panel), Equinox (March, April, September, and October: middle panel), and the December solstice (November, December, January, and February: bottom panel) periods. The F7/C2E1 IVM and ICON IVM have a uniform data distribution with respect to time.

Results and discussion

Diurnal variation of ion density

Figure 3 depicts the behavior of the ion density with local time. The diurnal variations of ion density are shown during June solstice (May, June, July, and August: middle panel), Equinox (March, April, September, and October: bottom panel), and December solstice (November, December, January, and February: top panel) during the solar minimum of the December 2019 to November 2020. The local time is binned by every hour, and the plot shows median ion density measured by F7/C2E1 (blue lines) and ICON (black lines). The ion density in the F region decreases at night and increases during the day, which is due to photoionization by solar EUV radiation and diurnal variations of the electromagnetic drifts (i.e., $E \times B$ drifts) that transport plasma to a higher altitude during the day and to lower altitude at night (e.g., Schunk and Nagy 1978, 2000; Anderson et al. 2004). The diurnal variation pattern of ion density is characterized by remarkable one peak pattern, occurring in the noon hours around 10:00–14:00 LT. The local time dependence of ion density measured by F7/C2E1 IVM is similar to that measured by ICON. The magnitude of ion

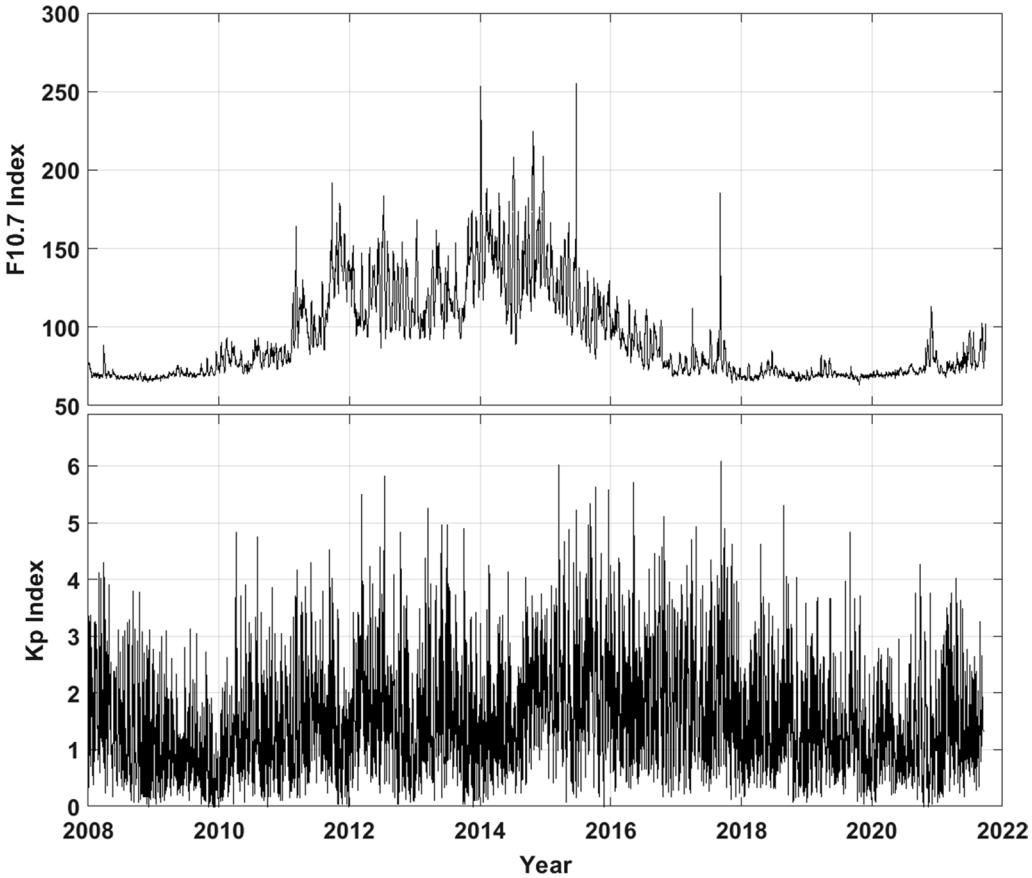

Fig. 1 The solar radio flux F10.7 and Kp index variations during 2008–2021

density during noon hours has a maximum value in the December solstice and a minimum value in the June solstice. Also, the ion density during Equinoxes is greater than that of June solstice. The ionosphere plasma density is determined by the plasma production, loss, and transport processes. Plasma production and loss are affected by EUV and recombination, respectively. Since the recombination is affected by thermospheric neutral density and the hemispheric wind effect, various factors drive the seasonal variation in plasma density. The difference in ion density resulting from the hemispheric wind effect is discussed in Fig. 4.

The ion density variation with local time is different depending on the season, and it also has a dependence on solar activity. In the diurnal variation of the ion density measured by F7/C2E1 and ICON during the low solar activity from December 2019 to November 2020, no increase in density due to pre-reversal enhancement (PRE) was observed. Xiong et al. (2016) reported the diurnal variation of electron density observed from Swarm A and C during moderate solar activity from April 2014 to April 2016. In their Fig. 4b, the electron density in the equinox measured by the Swarm increases rapidly near sunset (1700–1900 LT) because of the PRE effect. However, this characteristic is absent in the ion density measured by the in situ ion density observations of F7/C2E1 and ICON in this study.

The seasonal and solar activity variations of evening PRE have been reported by several literatures (Fejer et al. 1981, 1991, 2008; Kil et al. 2007, 2009). The PRE magnitude of the vertical plasma drift tends to increase with solar flux (Fejer et al. 1991, 1999; Kil et al. 2011b). The magnitude has also a dependence on seasonal variation, reaching its maximum during the equinox and its minimum during the June solstice (e.g., Fesen et al. 2000). The PRE can uplift the height of the equatorial F region, making a favorable condition for EPB development (e.g., Rajesh et al. 2017a). The reduced ion-neutral collision frequency at higher altitudes has a positive effect on the growth of Rayleigh–Taylor instability associated with EPB generation.

The solar activity dependence of the EPB occurrence probability was investigated based on the in situ satellite measurements of DMSP during 1989–2004

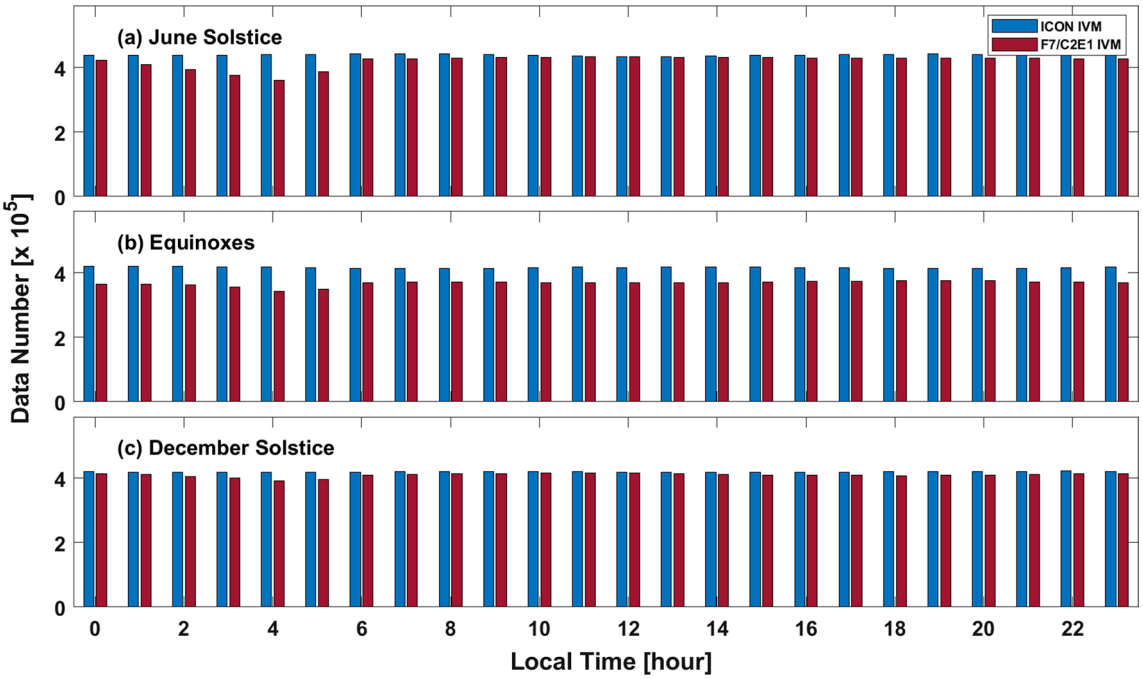

Fig. 2 Seasonal and local time distribution of data availability of F7/C2E1 and ICON during the solar minimum from December 2019 to November 2020 for three seasons

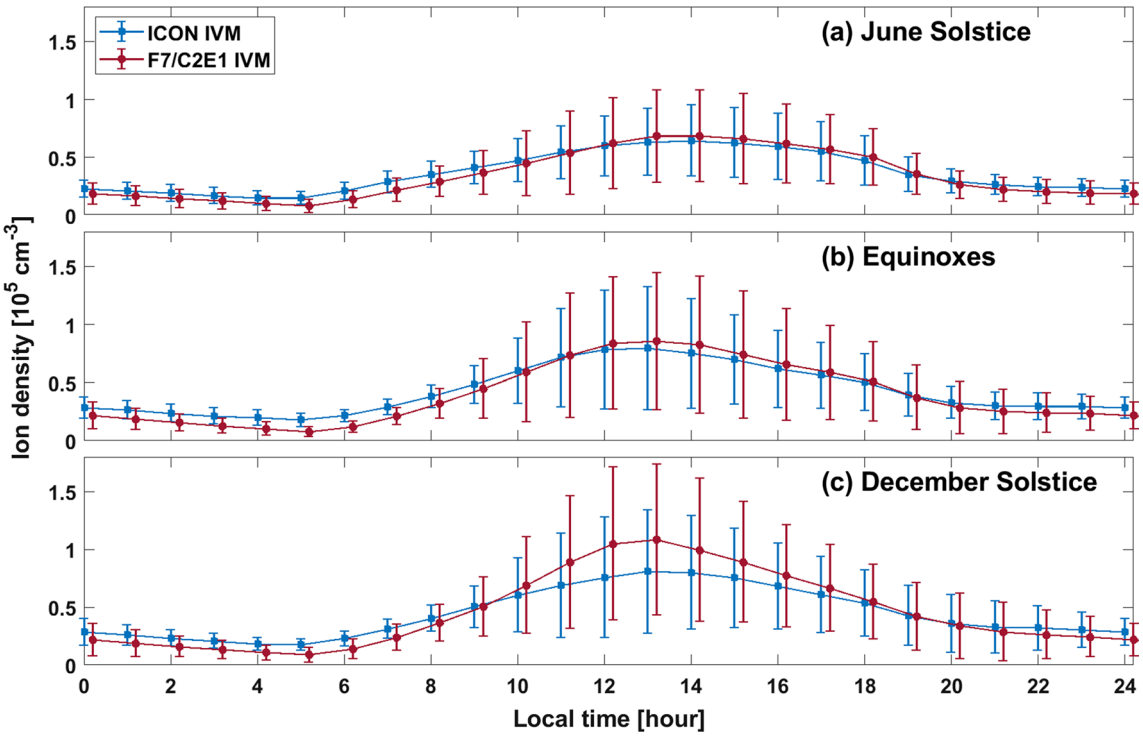

Fig. 3 Diurnal variations of the ion density observed by F7/C2E1 and ICON satellite during the solar minimum period (December 2019 to November 2020) for three seasons. The error bars indicate the median absolute deviation

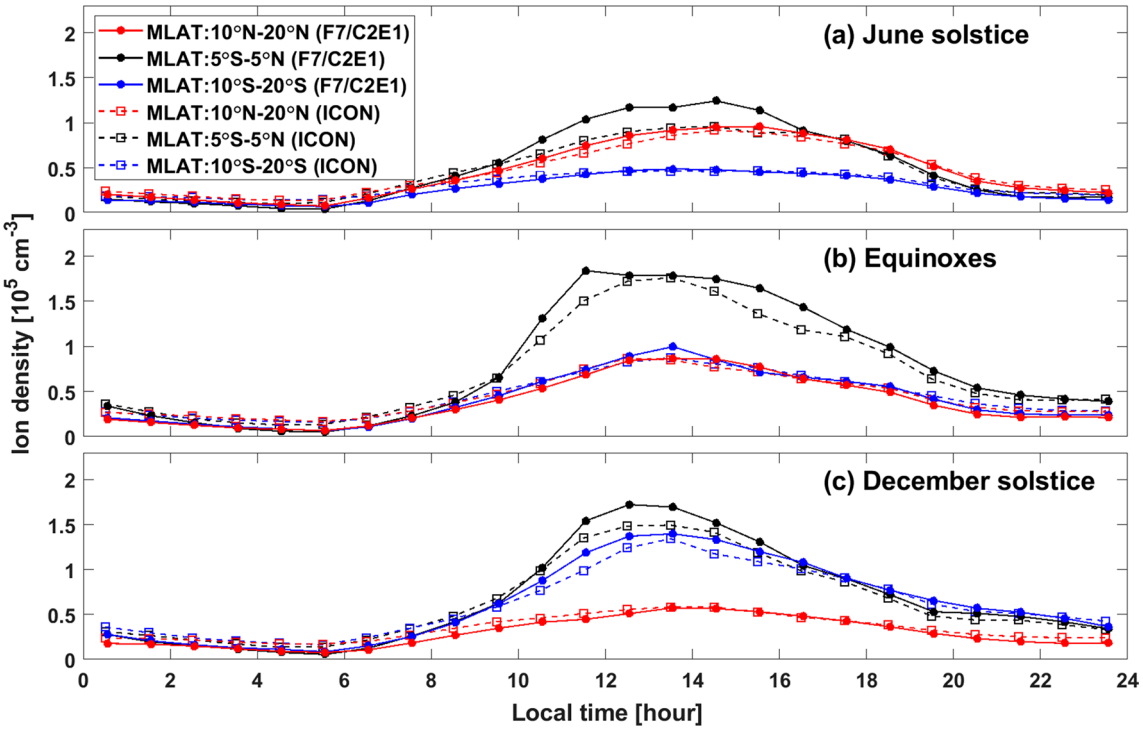

Fig. 4 Comparison of the averages of the observed ion densities by F7/C2E1 (blue) and ICON (black) at various magnetic latitude ranges for June solstice, Equinoxes, and December solstice

(Huang et al. 2002; Gentile et al. 2006) and C/NOFS during 2008–2014 (Huang et al. 2015) and CHAMP and GRACE during 2001–2009 (Xiong et al. 2010). EPBs occur more frequently at a higher solar activity. F7/C2 and ICON may observe relatively fewer EPBs during the solar minimum condition from December 2019 to November 2020, but they can still provide opportunities to study the evolutions of EPBs from lower to higher latitudes which correspond to lower to higher apex altitudes of the magnetic field lines. We will introduce an example of the EPB observed through the simultaneous observations of ICON and F7/C2 in "Simultaneous observations of equatorial plasma bubbles (EPBs)" section.

Figure 4 presents the local time variation of the averaged ion density for three different seasons at the equatorial (±5°) and low latitude (±10° to±20°) regions to characterize the structure of EIA. The averaged ion density measured by both satellites showed similar patterns regardless of latitude and seasonal variation. Coley et al. (2010) reported the ion density at an altitude of 500–550 km observed by C/NOFS IVM during the summer of 2008. The distribution of the equatorial ion density from both satellites agrees with those observed by C/NOFS IVM satellite.

Although the overall pattern is similar, the magnitude of densities at F7/C2E1 altitudes appear to be greater than or nearly identical to those of ICON. It can be seen from the figure that the two ion-densities differ mainly over the equatorial latitudes during 1000–1600 LT. This is the period when the equatorial plasma fountain is usually active, where the ExB force continuously re-distributes the vertical plasma density distribution over the equatorial latitudes. Under such dynamic control, an orbital difference of about 50 km between the ICON and F7/C2E1 missions could explain the observed difference in the corresponding ion-density measurements with the F7/C2E1 yielding slightly larger values. At low latitudes, this difference becomes negligible since the orbits of both the satellites are above the EIA crest locations.

ICON density in version 5 increases rapidly in the equatorial region of Equinox before 1800 LT (not shown here). However, this effect does not appear in version 6, which may indicate that the data reprocessing process is improving. We separated the data into the southern and northern hemispheres to compare the ion density distributions obtained from both satellites in low latitude regions. The low latitude F7/C2E1 and ICON densities between 12:00 and 14:00 LT exhibit more-or-less similar

distributions, except for a slight difference in the summer hemisphere in the solstice period.

The low-latitude plasma distributions by ICON and F7/C2 in Fig. 4 further reveal the signatures of hemisphere asymmetry and seasonal differences at the satellite altitudes. Since the summer-to-winter winds during solstice affects the plasma motion and ionospheric morphology (Rishbeth et al. 2000; Lin et al. 2007a, b), the F region neutral wind has a significant effect in the hemispheric asymmetry of the topside ionosphere. West et al. (1997) examined variations in ion composition associated with solar activity using DMSP F10 and concluded that F region neutral winds cause modulation of the F peak height, which is responsible for the hemispheric asymmetry of the topside ionosphere. Su et al. (1998) showed that the electron density obtained by the Hinotori satellite revealed an effect of ion drag on the meridional wind. Further, Kil et al. (2006) suggested that equatorial winds stand against downward plasma diffusion, resulting in hemispheric asymmetry of the topside ionosphere at an altitude of 840 km. The summer-to-winter winds are equatorward (poleward) at the summer (winter) hemisphere preventing (accelerating) the downward diffusion of the plasma at topside. The process results in stronger topside density at the summer hemisphere than the winter hemisphere. Kwak et al. (2019) presented the hemispheric asymmetry of EIA with solar cycle is associated with the fountain process and interhemispheric wind. In Fig. 4c, the density of the southern hemisphere (summer) is larger than those of the northern hemisphere (winter), which can be interpreted as the hemispheric wind effect during the December solstice. The summer and winter hemisphere asymmetry is more prominent during the December solstice than the June solstice, which is consistent with the annual asymmetry of the ionosphere (Millward et al. 1996; Rishbeth and Müller-Wodarg 2006). The more prominent annual asymmetry effect in the December solstice may cause differences in the density values of F7/C2E1 and ICON during the daytime (10–17 LT) in Fig. 3c. However, the hemispheric wind effect in the June solstice had less influence on the distribution of ion density compared to December (Figs. 3a, 4a).

The morphology of topside plasma density has been reported in several literatures, and it differs from the F peak height (Su et al. 1998; Kil et al. 2006; Liu et al. 2007). Figure 5 shows the distribution of averaged ion density on the topside F region (altitudes above F-peak) as a function of magnetic latitude observed by (left) F7/C2E1 and (right) ICON for three seasons. The ion density

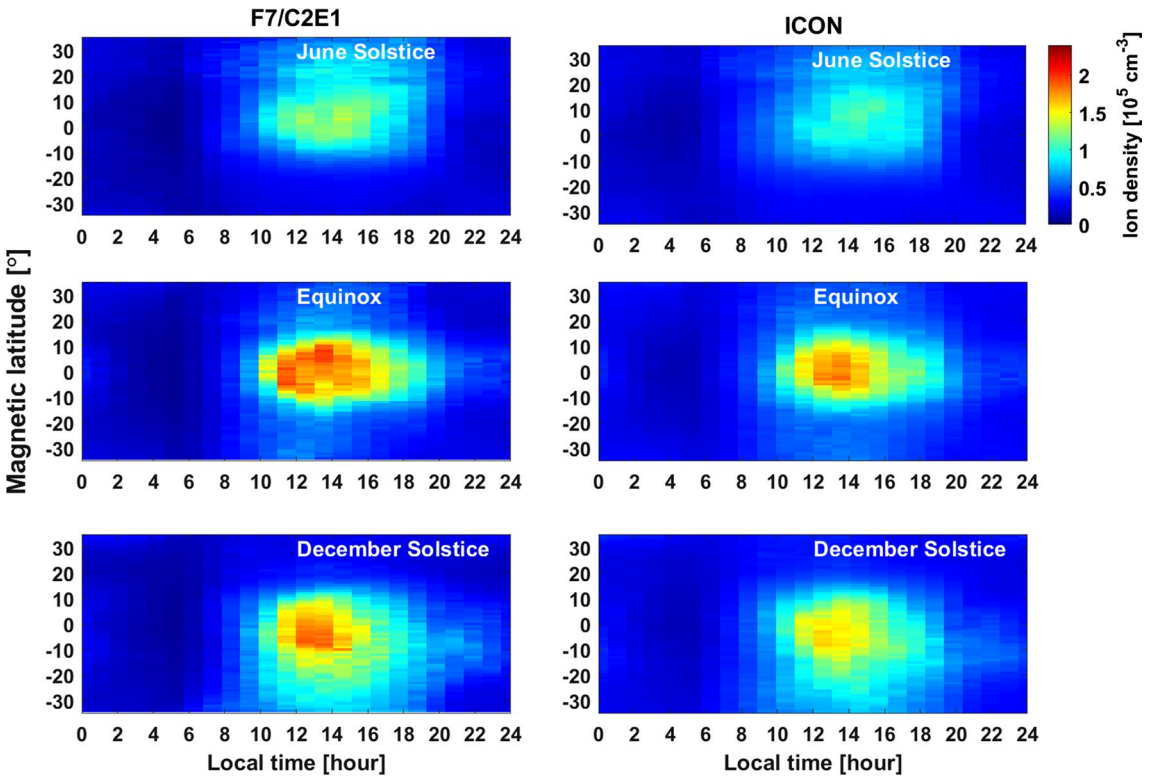

Fig. 5 The magnetic latitude and local time distributions of the topside average ion densities observed by F7/C2E1 and ICON

measurements from F7/C2E1 and ICON are sorted into local time (1 h) by magnetic latitude (5°) bins. The ion density at low latitude is higher during the Equinox and December solstice than during the June solstice. The topside ion density of ICON altitude and F7/C2E1 altitude did not show off-equatorial maxima in both hemispheres by the equatorial plasma fountain effect. The F7/C2E1 density has a similar distribution to the ICON density, but its amplitude appears to be stronger. Lee et al. (2011) investigated the F region electron density obtained from FORMOSAT-3/COSMIC in 2007 and showed that although the EIA peaks in both hemispheres were observed due to the fountain effect at the F peak height, the EIA structures of the southern and northern hemispheres at the 500 km altitude could not be clearly distinguished under solar minimum condition.

To understand the longitudinal variation of the ionosphere, we analyzed the median ion distribution at 12:00–1400 LT obtained from F7/C2E1 and ICON (Fig. 6). The magnetic latitude and geographic longitude are binned by 2° and 2°, respectively. The median density in each bin was calculated using data for June solstice (F7/C2E1: 122 days, ICON: 123 days), Equinox (F7/C2E1: 109 days, ICON: 120 days), and December solstice (F7/C2E1: 118 days, ICON: 119 days). Figure 6 shows that clear longitudinal variations with the wave number-4 structures in the satellite observations of ion density showing similar character as other satellite observations (e.g., Immel et al. 2006; Lin et al. 2007a; Lühr et al. 2008). Generally, F7/C2E1 IVM measures stronger ion density than ICON which is consistent with Figs. 3, 4, 5. The longitudinal variations show clear wave-4 pattern during the June solstice and equinox. This monthly variation of the wave-4 pattern is consistent with the previous topside density profile observation of radio occultation measurements reported by Lin et al. (2011). In December solstice, the wave-4 pattern becomes indiscernible, which again is consistent with the results of Lin et al. (2011).

The results are consistent with the nonmigrating diurnal tides in the neutral atmosphere according to the spectrum analysis of neutral temperature by Forbes et al. (2008). Their Fig. 2 shows the spectrum of the neutral temperature indicating the diurnal nonmigrating tide of eastward wavenumber-3 (or DE3), corresponding to wave-4 when viewed from global constant local time, is prominent during June and October. Their spectrum results also show some a weaker amplitude intensification of DE-3 around March. As per the results, the DE-3 has greater amplitudes over June solstices and equinox comparing to other months. For the December solstice

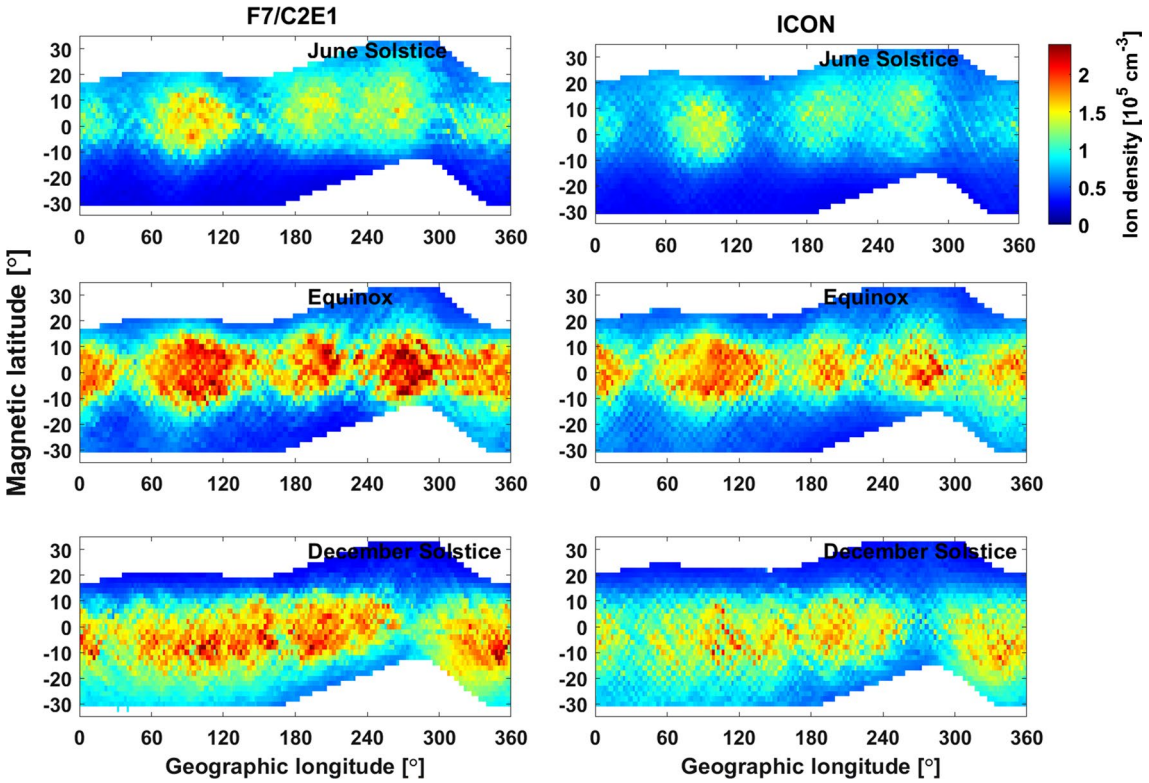

Fig. 6 The longitudinal ion density structures at 12:00–14:00 LT observed from ICON and F7/C2E1 for three seasons

period, there is a transition from DE-3 to DE-2 in the neutral temperature spectrum. As DE-2 contributes to wave-3 pattern in global constant local time, there should be a mixture of wave-3 and wave-4 around December solstice, which makes the longitudinal structure more complex during this season.

Simultaneous observations of equatorial plasma bubbles (EPBs)

In this section, we examine the observations of EPBs in the consecutive crossings of ICON and F7/C2 satellites on 18 October 2020. The ICON and F7/C2 altitudes on those days were near 600 km and 550 km, respectively. Figure 7 presents a series of four consecutive ion density measurements derived from ICON and F7/C2 satellites (named hereafter F7/C2E1-F7/C2E3), showing the spatial characteristics and time evolution of EPBs centered over Taiwan longitude sector in the post-sunset period. Figure 7a shows the longitude–latitude trajectories of ICON (blue), F7/C2E1 (magenta), F7/C2E2 (cyan), F7/C2E3 (yellow) passes during the period 12:00–13:00 UT (19:00–22:30 LT), and and that of F7/C2E4 (green) around 14:30 UT (21:30–00:00 LT). The black dashed line represents the magnetic equator. In Fig. 7b–e, the black curve is ion density measured by the IVM onboard each satellite. In order to calculate the smooth background density (red curve), we first applied a Savitzky–Golay low-pass filter (order = 3, window size = 51 data points). Then, the smoothing process was repeated for the low-pass filter values using 50 data points running average to remove small-scale fluctuations (e.g., Kil et al. 2011; Choi et al. 2017; Smith and Heelis 2018a, b).

The consecutive scans by the different IVMs in Fig. 7 enable the investigations of the evolution and characteristics of the EPBs over this region in the deep solar minimum conditions. The ICON IVM (Fig. 7b) detected a first group of EPBs (marked as EPB1) over 110°E at 12:38 UT near the magnetic equator. Note that no corresponding EPBs could be seen in the F7/C2E2 (Fig. 7d) pass over this region through low-latitudes in the northern hemisphere about 5 min earlier. This suggests that these are likely fresh irregularities developed over this region. Though F7/C2E3 (Fig. 7e) made measurements over this region a few minutes later, it was probably much away from the equator to detect these irregularities. On the other hand, based on the time and location of the EPBs and the similarity in their morphologies, the second (~ 115°E, 12:40 UT) and third (~ 127°E, 12:43 UT) groups of EPBs in the ICON scan are also likely detected by at least two other F7/C2 IVMs (marked as EPB2 and EPB3 in different panels). The EPB2 is first detected by F7/C2E1 around 11:57 UT, which also appears in the ICON and F7/C2E2 scans made about 35–45 min later, at slightly eastern longitudes. It is worth to note that the ICON and F7/C2E1 tracks were near equatorial latitudes when they observed EPB2, probably explaining their nearly identical patterns. However, F7/C2E2 detected EPB2 in the low-latitude region, more than 10° off the equator. Similarly, F7/C2E1 detected EPB3 around 12:01 UT near the magnetic equator, and about 45–50 min later, ICON and F7/C2E3 (Fig. 7e) measures the same EPB in the low-latitudes in the opposite hemispheres at slightly eastern longitudes. Note that F7/C2E3 also detected EPBs over these longitudes in a later pass after

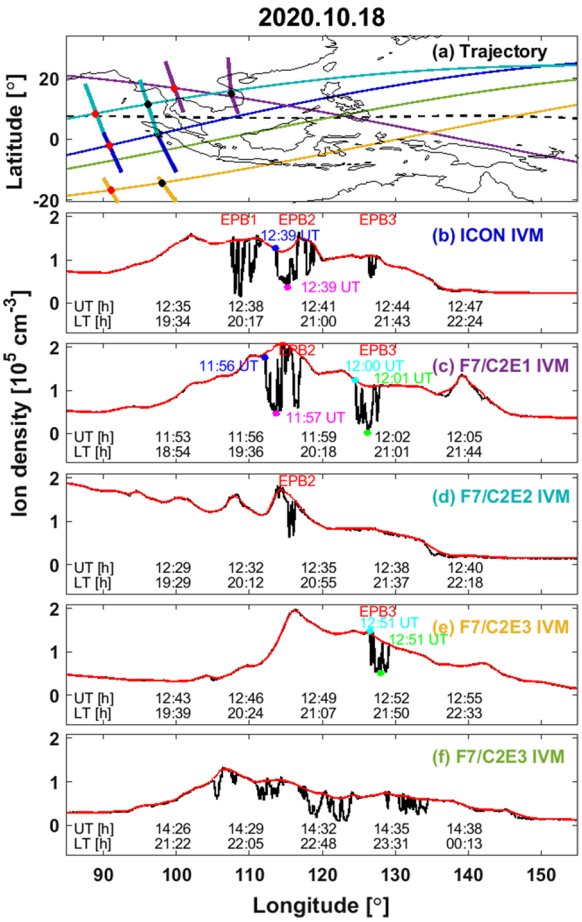

Fig. 7 The evolution of equatorial plasma bubbles measured by ICON and F7/C2 IVM around Taiwan on 18 October 2020. **a** Shows the ICON and F7/C2 orbits while the magnetic equator is shown with by black dashed line. The red and black points denote E- and F-region sunset terminator locations corresponding to the respective orbits, where the line segments through these points indicate the alignment of the terminator. The black and red curves indicate the measured ion density and calculated background density from **b** ICON IVM, **c** F7/C2E1 IVM, **d** F7/C2E2 IVM **e** F7/C2E3 IVM (~ 2100 LT), and **f** F7/C2E3 (~ 2200 LT), respectively. The blue, magenta and cyan dots indicate the west and east edges of EPB2 and the west edge of EPB3, respectively

about 2 h (Fig. 7f), suggesting that the EPB activity persisted for several hours with more irregularities being generated during the course of the night.

Such consecutive IVM measurements of the same EPB using multiple satellites at different longitudes and latitudes are extremely rare, and demonstrates the potential of the unique F7/C2 constellation and the concurrent ICON measurements in investigating the EPB characteristics. Since EPB2 is detected by ICON and F7/C2E1 at different longitudes over similar latitude region, the locations and measurement times (UT) are used to estimate the zonal drift velocity. The calculations yield a zonal drift of ~ 61 m/s at the western edge (blue dots in Fig. 7b and c) of EPB2 and ~ 67 m/s at the minimum value (magenta dots in Fig. 7b and c). Though EPB3 in F7C2E1 and F7C2E3 are detected at different latitudes, their structures appear similar. The average zonal speed at the western edge (cyan dots) and at the minimum value (green dots) are ~ 74 m/s and ~ 62 m/s, respectively. It should be noted that the estimated velocities only indicate the average drifts and are subject to the uncertainties associated with possible changes in the shape of EPB. Nevertheless, for relatively shorter time scales, the impact of such uncertainties is expected to be minimal and the observed values are generally consistent with the previous reports over East Asian sector in solar minimum conditions (e.g., Sarudin et al. 2020).

The multi-point observations depicted in Fig. 7 provide opportunity for further examination of the EPB evolution over magnetic equator as well as at low latitudes in conjugate hemispheres by projecting such measurements to corresponding apex altitudes. Figure 8 displays the apex altitudes of EPB2 and EPB3 in the different IVM measurements as a function of longitude. The EPB2 in ICON and F7/C2E1 are located approximately over similar apex altitudes of 590–648 km, and both reveal similar structure and are also identical in the strength of the ion density depletion. However, at the apex altitude of EPB2 in F7/C2E2 (~ 812 km) the irregularities appear much weaker compared to those at the lower altitude and only the leading (eastern) irregularities of these EPBs rise to these altitudes. Though F7/C2E3 (Fig. 6e) passed over this region a few minutes later with apex altitudes of ~ 1000 km, it did not detect EPB2.

Similarly, F7/C2E1 passes through EPB3 at an apex altitude of ~ 549 km, which had risen to about 749–778 km over the equator before being scanned by ICON and F7/C2E3 in conjugate hemispheres (Fig. 7). The strength of EPB3 in ICON has considerably weakened compared to that in F7/C2E1. However, despite being located at a similar apex altitude as that of the ICON, EPB3 strength in F7/C2E3 apparently changes only very little. This can be understood by examining the F7/C2E3 orbit in Figs. 7 and 8. Though F7/C2E3 initially detects EPB3 at about 10–12°S magnetic latitude (apex altitude of ~ 749 km), the subsequent portion of its orbit soon approaches latitudes closer to the equator (lower apex heights), where EPB3 is stronger.

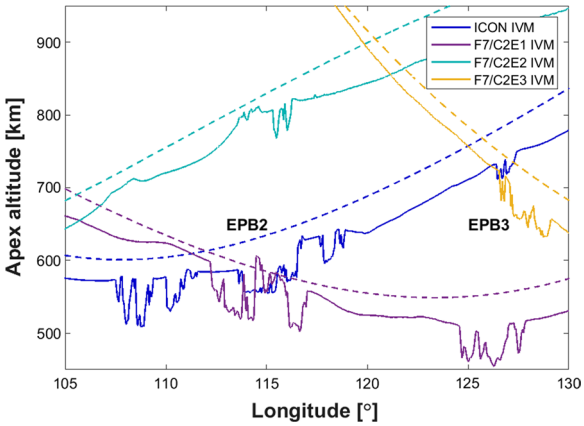

Fig. 8 The longitudinal variations of the apex height (solid lines) and ion density (dashed lines) mesured by the ICON, F7/C2E1, F7/C2E2, and F7/C2E3

Sun et al. (2016) reported that during low-moderate solar activity conditions, the apex altitudes of EPBs are generally limited within 725 km. By examining the climatology of EPBs using FORMOSAT-3/COSMIC measurements, Chou et al. (2020) showed that in the low solar flux period of 2008–2009, EPBs rarely rise above 600 km. The results above show irregularities rising to altitudes above 800 km in the solar minimum conditions. Though EPBs rise to relatively higher altitudes, their strength apparently decreases with height. For EPB3 in F7/C2E1 and ICON, observed about 43 min apart, the background ion densities outside the bubble are approximately in the comparable range. However, the strength of the bubble in F7/C2E1 is ~ 90%, whereas it is only ~ 45% in ICON. Thus, the bubble weakens by a factor or 2 when the apex altitude increased by about 210 km. The variation of the strength of the EPBs at different apex altitudes suggests that in the deep solar minimum conditions the irregularities already weaken by the time they rise to about 700–800 km altitude.

While the IVM scans in Fig. 6b–e made successive measurements of the same EPBs at different locations, enabling the estimation of zonal bubble drifts, the EPBs in the F7/C2E3 scan in Fig. 6f uniquely coincided with the all-sky imager by National Cheng Kung University at Tainan Astronomical and Educational Area (23.1°N, 120.4°E) in Taiwan (Rajesh et al. 2017b). Though the all-sky imager observations were restricted by cloudy weather in this night, the plasma bubbles structures could still be identified, overlapping with the IVM

measurement. Figure 9 presents the coincident observations of plasma bubble over Taiwan at (a) 22:30 LT and (b) 22:36 LT on the night of October 18, 2020. The airglow images in Fig. 9 are unwrapped into geographic coordinates, assuming an emission height of 250 km (Rajesh et al. 2017b). Two weak, but distinct plasma depletions could be detected in the airglow images within the pink dashed rectangles.

The F7/C2E3 orbit tracks (Fig. 6f) mapped to an altitude of 250 km along magnetic field lines and the corresponding ion density values are overplotted in Fig. 9 with green and red curves, respectively. Over the locations of the two plasma depletions, the IVM density also shows a corresponding decrease, confirming that both the observations detect the same EPBs. The airglow observations show that the maximum poleward latitude of the EPBs reach 22 N, corresponding to a maximum apex altitude of ~ 780 km. Though the sky conditions do not permit further quantitative comparisons of the two measurements, the concurrent observations displayed in Fig. 9 show the potential for more detailed investigations in future with the solar activity gradually rising.

To investigate the background ionospheric conditions when the EPBs occurred, the longitude–latitude maps of electron density at an altitude of 300 km obtained from the global ionosphere specifications (GIS) are shown in Fig. 10. GIS assimilates slant total electron contents (TECs) of ground-based GNSS and radio occultation of F7/C2 data (c.f. Lin et al. 2015, 2017, 2020) and reproduces three-dimensional global electron density distributions with 1-h time resolution. The previous 5-day average is used as reference day. The figure shows that on 18 October there was relatively stronger PRE compared to the reference. In panels (f) and (g), where the sunset terminator is around 120E, the EIA crests are stronger and more separated than the reference plots in (b) and (c). The corresponding differences in (f) and (k) further demonstrates the stronger EIA, showing enhanced electron density at the low latitudes. This is further evident in the latitudinal profiles of electron density at 120° E longitude and 300 km altitude in panels (m)-(p), where the magnitude of the crest density and the crest separation is larger on 18 October 2020.

Note that the diurnal pattern of the average ion-density by F7/C2 and ICON do not indicate any signature of PRE during 2019–2020 (Figs. 4, 5). Though not reflected in the average behavior, the GIS results demonstrate that the PRE on this day is relatively stronger. Further, according to the statistical observations of EPB occurrences during previous solar minimum periods, EPBs are mostly limited with about 700 km altitude (Sun et al. 2016; Chou et al. 2020). Though EPBs could develop from the turbulent background ionospheric structures, especially under high solar activity conditions as shown by Yokoyama et al. (2014) by using high-resolution numerical simulations, the stronger PRE on this day likely contributed in the observed EPBs that penetrated to apex altitudes above 800 km in the early ascending phase of the solar cycle 25.

Conclusions

In this paper, in situ ion density measurements from IVM onboard F7/C2E1 and ICON, respectively, are compared by using observations during magnetic quiet days of the solar minimum period from December 2019 to November 2020. The diurnal variation of ion density of the F7/C2E1 is similar to that of ICON for the three seasons. The daytime electron density has maxima around the December solstice and minima around the June solstice. The density of both satellites at the equatorial region

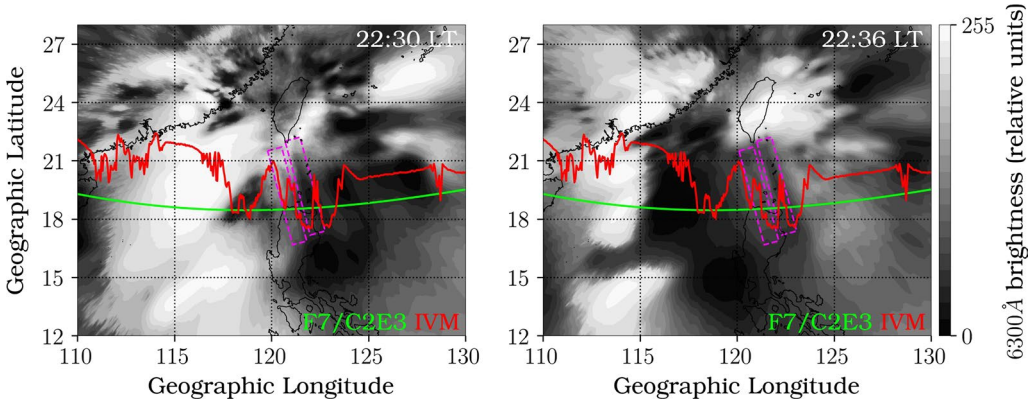

Fig. 9 Simultaneous observations of unwarped OI 630.0 nm airglow images with the ion density of F7/C2E3 (left) at 22:30 LT and (right) at 22:36 LT on 18 October 2020. The green and red curves indicate the F7/C2E3 orbit and ion density, respectively. The locations of the two weak plasma depletions in the images are highlighted using dashed rectangles

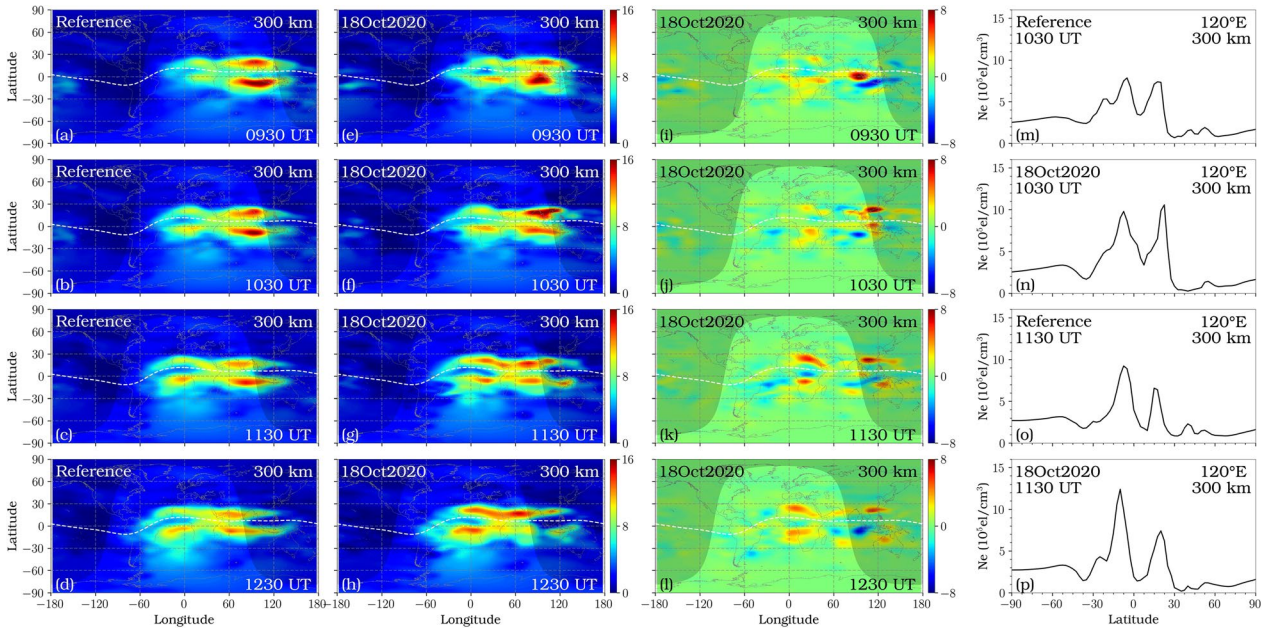

Fig. 10 The longitude–latitude maps of electron density at an altitude of 300 km obtained from the F7/C2 GIS data during 0930–1230 UT. **a**–**d** The average electron density during previous 5 days as reference. **e**–**h** The electron density on 18 October 2020. **i**–**l** the difference between the two. The white dotted line denotes the geomagnetic equator and the shaded region corresponds to post-sunset period. The latitude profiles of electron density at selected periods of 1030 and 1130 UT at 120 E longitude on 18 October 2020 are shown in **n** and **p** to compare the PRE on this day with that on the reference day in **m** and **o**

did not show any effect by PRE during the solar minimum period (December 2019 to November 2020). Both the observations show hemispheric asymmetry in the topside ion density, which is pronounced in December solstice compared to June solstice. The longitudinal distribution further shows the characteristic wavenumber-4 pattern, which is prominent in June solstice and equinox months, and is weaker in December solstice. The consecutive passes of F7/C2 and ICON IVMs detect the evolution of the same EPBs at different longitudes and latitudes (apex altitudes), showing eastward drift velocities of 60–70 m/s. The EPBs rise to apex altitudes of over 800 km, which is rare in the deep solar minimum conditions and the electron density measurements from F7/C2 GIS indicate that stronger PRE on this day likely contribute in their generation. The results show that such consecutive IVM orbits provide potential for detecting the evolution of the EPBs in a given region to identify the characteristics, and further compare with concurrent all sky imager observations. The F7/C2 IVM and ICON IVM provide topside ion density with good performance, and this is confirmed in this study through the statistical analysis and an event study. The ion density data from the F7/C2 IVM and ICON IVM provide opportunities for understanding the characteristics of ionospheric irregularity and its evolution during the solar minimum.

Acknowledgements
JC thanks the ICON Team for providing IVM observations.

Author contributions
JMC conducted data analysis and wrote the first draft of the manuscript. CCL designed this study and helped the interpretation of the results. RPK supported the Taiwan all-sky imager data analysis. JHP supported the satellites data analysis and discussion of data characteristics. YSK contributed to the interpretation of the results. SPC managed the F7/C2 satellite data and helped the data analysis. JTL operated the Taiwan all-sky imager. MTC provided all logistics and support for installing and maintaining the all-sky imager. All authors read and approved the final manuscript.

Funding
This work is partly supported by the Ministry of Science and Technology under MOST 111–2111-M-006–001 and MOST 111–2119-M-006–001, National Space Organization under NSPO-S-110296, and the Headquarter of University Advancement at National Cheng Kung University, which is sponsored by the Taiwan Ministry of Education under grant number D111-G2205. J. Park and Y.-S. Kwak were supported by basic research funding from the Korea Astronomy and Space Science Institute (KASI) (KASI2022185009).

Availability of data and materials
The F7/C2 IVM data are downloaded from the website of the Taiwan Analysis Center for COSMIC (TACC, https://tacc.cwb.gov.tw/data-service/fs7_provisional/level2/ivmL2m/) or the University Corporation for Atmospheric Research (UCAR, https://data.cosmic.ucar.edu/gnss-ro/cosmic2/postProc/level2/). The ICON IVM data are available from ftp://icon-science.ssl.berkeley.edu/pub/LEVEL.2/IVM-A/. F10.7 and Kp index were obtained from the OMNIWEB database (https://omniweb.gsfc.nasa.gov/ow.html). Access to all sky images is at http://allsky-airglow.earth.ncku.edu.tw/PicWeb/MainHTML/2020/10/18.

Declarations

Competing interests
The authors declare that they have no conflict of interest.

Author details
[1]Department of Earth Sciences, National Cheng Kung University, Tainan, Taiwan. [2]Korea Astronomy and Space Science Institute, Daejeon, South Korea. [3]University of Science and Technology, Daejeon, South Korea. [4]Taiwan Astronomical Educational Area, Tainan, Taiwan.

Received: 16 June 2022 Accepted: 22 December 2022
Published online: 28 January 2023

References
Anderson D, Anghel A, Chau JL, Veliz O (2004) Daytime vertical E × B drift velocities inferred from ground-based magnetometer observations at low latitudes. Space Weather 2:S11001. https://doi.org/10.1029/2004SW000095

Chen Y, Liu L, Wan W (2011) Does the F10.7 index correctly describe solar EUV flux during the deep solar minimum of 2007–2009? J Geophys Res 116:A04304. https://doi.org/10.1029/2010JA016301

Chen C-H, Tsai H-F, Wang L-Y, Lin C-HC, Liu J-Y, Yeh W-H (2021) The comparison of topmost radio occultation electron densities with in-situ ion densities from FORMOSAT-7/COSMIC-2. Terr Atmos Ocean Sci 32:953–958. https://doi.org/10.3319/TAO.2021.07.26.01

Choi J-M, Kil H, Kwak Y-S, Park J, Lee WK, Kim YH (2017) Periodicity in the occurrence of equatorial plasma bubbles derived from the C/NOFS observations in 2008–2012. J Geophys Res Space Physics 122:1137–1145. https://doi.org/10.1002/2016JA023528

Chou M-Y, Wu Q, Pedatella NM, Cherniak I, Schreiner WS, Braun J (2020) Climatology of the equatorial plasma bubbles captured by FORMOSAT-3/COSMIC. J Geophys Res Space Phys 125(5):e2019JA027680. https://doi.org/10.1029/2019JA027680

Chou M-Y, Braun JJ, Wu Q, Heelis RA, Zakharenkova I, Cherniak I, Pedatella NM, Stoneback RA (2021a) Validation of FORMOSAT-7/COSMIC2 IVM ion density and TGRS orbit electron density. Terr Atmos Ocean Sci 32:939–951. https://doi.org/10.3319/TAO.2021.06.22.01

Chou M-Y, Lin CCH, Huba JD (2021b) Modeling the disappearance of equatorial plasma bubble by nighttime medium-scale traveling ionospheric disturbances. Terr Atmos Ocean Sci 32:217–228. https://doi.org/10.3319/TAO.2021.03.30.01

Chu C-H, Huang C-Y, Fong C-J, Chen S-Y, Chen Y-H, Yeh W-H, Kuo Y-H (2021) Atmospheric remote sensing using global navigation satellite systems: From FORMOSAT-3/COSMIC to FORMOSAT-7/COSMIC-2. Terr Atmos Ocean Sci 32:1001–1013. https://doi.org/10.3319/TAO.2021.11.15.02

Coley WR, Heelis RA, Hairston MR, Earle GD, Perdue MD, Power RA, Harmon LL, Holt BJ, Lippincott CR (2010) Ion temperature and density relationships measured by CINDI from the C/NOFS spacecraft during solar minimum. J Geophys Res 115:A02313. https://doi.org/10.1029/2009JA014665

Derghazarian S, Hysell DL, Varney RH (2021) Topside measurements at Jicamarca during the 2019–2020 deep solar minimum. J Geophys Res 126:e2021JA029695. https://doi.org/10.1029/2021JA029695

Emmert JT, Lean JL, Picone JM (2010) Record low thermospheric density during the 2008 solar minimum. Geophys Res Lett 37:L12102. https://doi.org/10.1029/2010GL043671

Fejer BG, Farley DT, Gonzales CA, Woodman RF, Calderon C (1981) F region east-west drifts at Jicamarca. J Geophys Res 86(A1):215–218. https://doi.org/10.1029/JA086iA01p00215

Fejer BG, de Paula ER, Gonzales SA, Woodman RF (1991) Average vertical and zonal F region plasma drifts over Jicamarca. J Geophys Res 96(A8):13901–13906. https://doi.org/10.1029/91JA01171

Fejer BG, Scherliess L, de Paula ER (1999) Effects of the vertical plasma drift velocity on the generation and evolution of equatorial spread F. J Geophys Res 104(A9):19859–19869. https://doi.org/10.1029/1999JA900271

Fejer BG, Jensen JW, Su SY (2008) Quiet time equatorial F region vertical plasma drift model derived from ROCSAT-1 observations. J Geophys Res 113:A05304. https://doi.org/10.1029/2007JA012801

Fesen CG, Crowley G, Roble RG, Richmond AD, Fejer BG (2000) Simulation of the pre-reversal enhancement in the low latitude vertical ion drifts. Geophys Res Lett 27(13):1851–1854. https://doi.org/10.1029/2000GL000061

Forbes JM, Zhang X, Palo S, Russell J, Mertens CJ, Mlynczak M (2008) Tidal variability in the ionospheric dynamo region. J Geophys Res 113:A02310. https://doi.org/10.1029/2007JA012737

Gentile LC, Burke WJ, Rich FJ (2006) A climatology of equatorial plasma bubbles from DMSP 1989–2004. Radio Sci 41:RS5S21. https://doi.org/10.1029/2005RS003340

Heelis RA, Coley WR, Burrell AG, Hairston MR, Earle GD, Perdue MD, Power RA, Harmon LL, Holt BJ, Lippincott CR (2009) Behavior of the O+/H+ transition height during the extreme solar minimum of 2008. Geophys Res Lett 36:L00C03. https://doi.org/10.1029/2009GL038652

Heelis RA, Stoneback RA, Perdue MD, Depew MD, Morgan WA, Mankey MW et al (2017) Ion velocity measurements for the ionospheric connections explorer. Space Sci Rev 212:615–629. https://doi.org/10.1007/s11214-017-0383-3

Hei MA, Bernhardt PA, Siefring CL, Wilkens MR, Huba JD, Krall JF, Valladares CE, Heelis RA, Hairston MR, Coley WR, Chau JL, de La Jara C (2014) Radio-tomographic images of postmidnight equatorial plasma depletions. Geophys Res Lett 41:13–19. https://doi.org/10.1002/2013GL056112

Huang C-S (2017) The characteristics and generation mechanism of small-amplitude and large-amplitude ESF irregularities observed by the C/NOFS satellite. J Geophys Res Space Phys 122:8959–8973. https://doi.org/10.1002/2017JA024041

Huang C-S, Hairston MR (2015) The postsunset vertical plasma drift and its effects on the generation of equatorial plasma bubbles observed by the C/ NOFSsatellite. J Geophys Res Space Physics 120:2263–2275. https://doi.org/10.1002/2014JA020735

Huang CY, Burke WJ, Machuzak JS, Gentile LC, Sultan PJ (2002) Equatorial plasma bubbles observed by DMSP satellites during a full solar cycle: Toward a global climatology. J Geophys Res 107(A12):1434. https://doi.org/10.1029/2002JA009452

Huang C-S, de La Beaujardière O, Roddy PA, Hunton DE, Ballenthin JO, Hairston MR, Pfaff RF (2013) Large-scale quasiperiodic plasma bubbles: C/NOFS observations and causal mechanism. J Geophys Res Space Physics 118:3602–3612. https://doi.org/10.1002/jgra.50338

Huang C-S, de La Beaujardiere O, Roddy PA, Hunton DE, Liu JY, Chen SP (2014) Occurrence probability and amplitude of equatorial ionospheric irregularities associated with plasma bubbles during low and moderate solar activities (2008–2012). J Geophys Res Space Phys 119:1186–1199. https://doi.org/10.1002/2013JA019212

Immel TJ, Sagawa E, England SL, Henderson SB, Hagan ME, Mende SB, Frey HU, Swenson CM, Paxton LJ (2006) Control of equatorial ionospheric morphology by atmospheric tides. Geophys Res Lett 33:L15108. https://doi.org/10.1029/2006GL026161

Immel TJ, England SL, Mende SB, Heelis RA, Englert CR, Edelstein J, Sirk MM (2018) The ionospheric connection explorer mission: Mission goals and design. Space Sci Rev 214(1):13. https://doi.org/10.1007/s11214-017-0449-2

Immel TJ, Harding BJ, Heelis RA et al (2021) Regulation of ionospheric plasma velocities by thermospheric winds. Nat Geosci 14:893–898. https://doi.org/10.1038/s41561-021-00848-4

Kelley MC (2009) The Earth's ionosphere: Plasma physics and electrodynamics. Elsevier, Oxford

Kil H, Oh S-J (2011) Dependence of the evening prereversal enhancement of the vertical plasma drift on geophysical parameters. J Geophys Res 116:A05311. https://doi.org/10.1029/2010JA016352

Kil H, Su S-Y, Paxton LJ, Wolven BC, Zhang Y, Morrison D, Yeh HC (2004) Coincident equatorial bubble detection by TIMED/GUVI and ROCSAT-1. Geophys Res Lett 31:L03809. https://doi.org/10.1029/2003GL018696

Kil H, DeMajistre R, Paxton LJ, Zhang Y (2006) Nighttime Fregion morphology in the low and middle latitudes seen from DMSP F15 and TIMED/GUVI. J Atmos Sol Terr Phys 68:1672–1681. https://doi.org/10.1016/j.jastp.2006.05.024

Kil H, Oh S-J, Kelley MC, Paxton LJ, England SL, Talaat E, Min K-W, Su S-Y (2007) Longitudinal structure of the vertical E × B drift and ion density from ROCSAT-1. Geophys Res Lett 34:L14110. https://doi.org/10.1029/2007GL030018

Kil H, Paxton LJ, Oh S-J (2009) Global bubble distribution seen from ROCSAT-1 and its association with the evening prereversal enhancement. J Geophys Res 114:A06307. https://doi.org/10.1029/2008JA013672
Kil H, Choi H-S, Heelis RA, Paxton LJ, Coley WR, Miller ES (2011) Onset conditions of bubbles and blobs: A case study on 2 March 2009. Geophys Res Lett 38:L06101. https://doi.org/10.1029/2011GL046885
Kil H, Kwak Y-S, Lee WK, Miller ES, Oh S-J, Choi H-S (2015) The causal relationship between plasma bubbles and blobs in the low-latitude F region during a solar minimum. J Geophys Res Space Phys 120:3961–3969. https://doi.org/10.1002/2014JA020847
Kwak YS, Kil H, Lee WK, Yang T-Y (2019) Variation of the hemispheric asymmetry of the equatorial ionization anomaly with solar cycle. J Astron Space Sci 36(3):159–168. https://doi.org/10.5140/JASS.2019.36.3.159
Lee WK, Kil H, Kwak Y-S, Wu Q, Cho S, Park JU (2011) The winter anomaly in the middle-latitude F region during the solar minimum period observed by the Constellation Observing System for Meteorology, Ionosphere, and Climate. J Geophys Res 116:A02302. https://doi.org/10.1029/2010JA015815
Lin CH, Liu JY, Fang TW, Chang PY, Tsai HF, Chen CH, Hsiao CC (2007a) Motions of the equatorial ionization anomaly crests imaged by FORMOSAT-3/COSMIC. Geophys Res Lett 34:L19101. https://doi.org/10.1029/2007GL030741
Lin CH, Hsiao CC, Liu JY, Liu CH (2007b) Longitudinal structure of the equatorial ionosphere: time evolution of the four-peaked EIA structure. J Geophys Res 112:A12305. https://doi.org/10.1029/2007JA012455
Lin CY, Matsuo T, Liu JY, Lin CH, Tsai HF, Araujo-Pradere EA (2015) Ionospheric assimilation of radio occultation and ground-based GPS data using non-stationary background model error covariance. Atmos Meas Tech 8(1):171–182. https://doi.org/10.5194/amt-8-171-2015
Lin CY, Matsuo T, Liu JY, Lin CH, Huba JD, Tsai HF, Chen CY (2017) Data assimilation of ground-based GPS and radio occultation total electron content for global ionospheric specification. J Geophys Res Space Phys. https://doi.org/10.1002/2017JA024185
Lin C-Y, Lin CC-H, Liu J-Y et al (2020) The early results and validation of FORMOSAT-7/COSMIC-2 space weather products: Global ionospheric specification and Ne-aided Abel electron density profile. J Geophys Res Space Phys 125:1–12. https://doi.org/10.1029/2020JA028028
Lin CH, Chen CH, Tsai FH, Liu CH, Liu YJ, Kakinami Y (2011). Longitudinal Structure of the Mid- and Low-Latitude Ionosphere Observed by Space-borne GPS Receivers, Aeronomy of the Earth's Atmosphere and Ionosphere, Chapter 27, pp. 363–374, IAGA SPECIAL SOPRON BOOK SERIES Volume 2, Springer, doi: https://doi.org/10.1007/978-94-007-0326-1_27
Liu L, Wan W, Yue X, Zhao B, Ning B, Zhang M-L (2007) The dependence of plasma density in the topside ionosphere on solar activity level. Ann Geophys 25(6):1337–1343. https://doi.org/10.5194/angeo-25-1337-2007
Liu L, Le H, Chen Y, He M, Wan W, Yue X (2011) Features of the middle- and low-latitude ionosphere during solar minimum as revealed from COSMIC radio occultation measurements. J Geophys Res 116:A09307. https://doi.org/10.1029/2011JA016691
Lühr H, Xiong C (2010) IRI-2007 model overestimates electron density during the 23/24 solar minimum. Geophys Res Lett 37:L23101. https://doi.org/10.1029/2010GL045430
Lühr H, Rother M, HauslerAlkenMaus KPS (2008) The influence of nonmigrating tides on the longitudinal variation of the equatorial electrojet. J Geophys Res 113:A08313. https://doi.org/10.1029/2008JA013064
Martinis C, Mendillo M (2007) Equatorial spread F-related airglow depletions at Arecibo and conjugate observations. J Geophys Res 112:A10310. https://doi.org/10.1029/2007JA012403
Millward GH, Rishbeth H, Fuller-Rowell TJ, Aylward AD, Quegan S, Moffett RJ (1996) Ionospheric f 2 layer seasonal and semiannual variations. J Geophys Res 101(A3):5149–5156. https://doi.org/10.1029/95JA03343
Rajesh PK, Lin CH, Chen CH, Lin JT, Matsuo T, Chou MY, Chen WH, Chang MT, You CF (2017a) Equatorial plasma bubble generation/inhibition during 2015 St. Patrick's Day storm. Space Weather. https://doi.org/10.1002/2017aSW001641
Rajesh PK, Lin CH, Chen CH, Chen WH, Lin JT, Chou MY, Chang MT, You CF (2017b) Global equatorial plasma bubble growth rates using ionosphere data assimilation. J Geophys Res Space Physics 122:3777–3787. https://doi.org/10.1002/2017JA023968
Rishbeth H, Müller-Wodarg ICF (2006) Why is there more ionosphere in January than in July? The annual asymmetry in the F2-layer. Ann Geophys 24:3293–3311. https://doi.org/10.5194/angeo-24-3293-2006
Rishbeth H, Müller-Wodarg ICF, Zou L, Fuller-Rowell TJ, Millward GH, Moffett RJ et al (2000) Annual and semiannual variations in the ionospheric F2-layer: II. Physical Discussion. Ann Geophys 18(8):945–956. https://doi.org/10.1007/s00585-000-0945-6
Sarudin I, Hamid NSA, Abdullah M, Buhari SM, Shiokawa K, Otsuka Y, Yatini CY (2020) Equatorial plasma bubble zonal drift velocity variations in response to season, local time, and solar activity across Southeast Asia. J Geophys Res Space Phys 125:e2019JA027521. https://doi.org/10.1029/2019JA027521
Schunk RW, Nagy AF (1978) Electron temperatures in the F region of the ionosphere: Theory and observations. Rev Geophys 15:355–399
Schunk RW, Nagy AF (2000) Ionospheres, Physics, Plasma Physics and Chemistry. Cambridge, New York, pp 254–264
Smith JM, Heelis RA (2018a) The plasma environment associated with equatorial ionospheric irregularities. J Geophys Res Space Physics 123:1583–1592. https://doi.org/10.1002/2017JA024933
Smith JM, Heelis RA (2018b) Plasma dynamics associated with equatorial ionospheric irregularities. Geophys Res Lett. https://doi.org/10.1029/2018GL078560
Solomon SC, Woods TN, Didkovsky LV, Emmert JT, Qian L (2010) Anomalously low solar extreme-ultraviolet irradiance and thermospheric density during solar minimum. Geophys Res Lett 37:L16103. https://doi.org/10.1029/2010GL044468
Su YZ, Bailey GJ, Oyama K-I (1998) Annual and seasonal variations in the low-latitude topside ionosphere. Ann Geophys 16:974–985. https://doi.org/10.1007/s00585-998-0974-0
Su S-Y, Liu CH, Ho HH, Chao CK (2006) Distribution characteristics of topside ionospheric density irregularities: Equatorial versus midlatitude regions. J Geophys Res 111:A06305. https://doi.org/10.1029/2005JA011330
Sultan PJ (1996) Linear theory and modeling of the Rayleigh-Taylor instability leading to the occurrence of equatorial spread F. J Geophys Res 101(A12):875–926. https://doi.org/10.1029/96JA00682
Sun L, Xu J, Wang W, Yuan W, Li Q, Jiang C (2016) A statistical analysis of equatorial plasma bubble structures based on an all-sky airglow imager network in China. J Geophys Res Space Phys 121(11):11495–11517. https://doi.org/10.1002/2016JA022950
West KH, Heelis RA, Rich FJ (1997) Solar activity variations in the composition of the low-latitude topside ionosphere. J Geophys Res 102(A1):295–305. https://doi.org/10.1029/96JA03031
Xiong C, Park J, Lühr H, Stolle C, Ma SY (2010) Comparing plasma bubble occurrence rates at CHAMP and GRACE altitudes during high and low solar activity. Ann Geophys 28:1647–1658. https://doi.org/10.5194/angeo-28-1647-2010
Xiong C, Zhou Y-L, Lühr H, Ma S-Y (2016) Diurnal evolution of the F region electron density local time gradient at low and middle latitudes resolved by the Swarm constellation. J Geophys Res Space Phys 121:9075–9089. https://doi.org/10.1002/2016JA023034
Yizengaw E, Moldwin MB, Sahai Y, de Jesus R (2009) Strong postmidnight equatorial ionospheric anomaly observations during magnetically quiet periods. J Geophys Res 114:A12308. https://doi.org/10.1029/2009JA014603
Yizengaw E, Retterer J, Pacheco EE, Roddy P, Groves K, Caton R, Baki P (2013) Postmidnight bubbles and scintillations in the quiet-time June solstice. Geophys Res Lett 40:5592–5597. https://doi.org/10.1002/2013GL058307
Yokoyama T, Shinagawa H, Jin H (2014) Nonlinear growth, bifurcation and pinching of equatorial plasma bubble simulated by three-dimensional high-resolution bubble model. J Geophys Res Space Phys 119:10474–10482. https://doi.org/10.1002/2014JA020708

Publisher's Note